HIGH SPATIAL RESOLUTION MICROWAVE OBSERVATIONS OF THE SUN

M. R. KUNDU

Astronomy Program, University of Maryland, College Park, MD 20742, U.S.A.

Abstract. Over the past decade two large arrays – the Westerbork Synthesis Radio Telescope (WSRT) and the Very Large Array (VLA) built primarily for sidereal radio astronomy have been used for solar radio astronomical studies with spatial resolution of a few seconds of arc. In this review, we discuss some results obtained at Maryland using these instruments.

The quiet Sun observations made with the WSRT have premitted us to produce synthesized maps of supergranulation network at 6 cm wavelength. The brightness temperatures of typical network elements and cells are respectively $\sim 2.5 \times 10^4$ K and $\sim 1.5 \times 10^4$ K; thus the contrast is 1.7:1 which compares with 1.3:1 for Ca^+K and 2:0 for Lα networks. Limb profiles in both equatorial and polar directions have been obtained; limb brightening is observed at both west and south limbs, peak limb temperature being about 40% higher than disk temperature. We have produced synthesized maps of disk filaments which correspond well to Hα disk filaments and regions of reduced emission in He I 10 830 Å spectroheliograms. Using the WSRT synthesized maps at 6 cm, we have compared the structure of a sunspot associated source with model computations. Using a new method of analysis we have been able to map the vertical as well as the horizontal component of the sunspot magnetic field at specific locations in the low corona. Using the VLA, we have mapped coronal loops at 20 cm; the radio emission is attributed to bremsstrahlung near the loop footpoints whereas gyroresonance process dominates near the loop top. Using the VLA, we have carried out simultaneous observations of a microwave burst at 2 and 6 cm. The 6 cm burst source is apparently located near the top of a flaring loop, while the 2 cm emission originates from the loop footpoints. The 6 cm emission is attributed to gyrosynchrotron radiation of thermal electons in the bulk heated plasma at $\sim 4 \times 10^7$ K, while the 2 cm emission is due to nonthermal particles released and accelerated during the flare process. A DC electric field flare model appears to explain the observed delay between the peaks at the two wavelengths. From the delay, the strength of the electric field in the flaring region is estimated.

1. Introduction

Over the past two decades, several large synthesis arrays have been built, primarily for studies in sidereal radio astronomy. Two of these arrays, namely the Westerbork Synthesis Radio Telescope (WSRT) in the Netherlands and the Very Large Array (VLA) in the U.S.A. have been used in a limited manner for solar radio astronomy. These arrays provide spatial resolution ranging from $\sim 1''$ to $10''$ at centimeter wavelengths. Since the radio emission at these wavelengths originates from the upper chromosphere, the transition region and the corona, it is a useful probe for the temperature and density in these regions. The radio emission from active and flaring regions at these wavelengths is strongly influenced by the magnetic fields and, therefore, can be used to estimate the magnetic fields in these regions. In particular, synthesized maps in total intensity and circular polarization obtained with a spatial resolution of $\lesssim 1''$ arc offer a powerful tool for probing the magnetic field topology in the active and flaring regions. Since the flare energy release takes place at lower levels of the solar atmosphere, such maps taken at short time intervals should allow us to test different flare models. In this review, we present some results obtained at Maryland with the WSRT and VLA on the

Solar Physics **100** (1985) 491–514. 0038–0938/85.15.

quiet Sun (supergranulation network and limb profile), active regions (sunspot-associated regions and coronal loops) and flaring regions.

2. Quiet Sun Observations with the WSRT

High-resolution radio observations of the quiet Sun provide valuable information on the structure of the solar atmosphere and on other quiet Sun phenomena such as the supergranulation network and quiescent prominences. Kundu *et al.* (1979) observed the Sun at 6 cm with the Westerbork Synthesis Radio Telescope (WSRT) during the period 1976, June 15–18 when the solar activity was near minimum. The two main objectives of the observations were to study the supergranulation network and the limb brightening at radio frequencies.

The supergranulation network which is associated with convective circulation at and below the photosphere is clearly seen at visible and ultraviolet wavelengths. The temperature and density of the network are believed to be determined primarily by the magnetic fields which are concentrated at the edges of the cells by convective motions. Since the radio emission is generated by free-free emission from the thermal plasma, it is possible that, by mapping the supergranulation network at radio wavelengths, one can study the temperature and density within the cell center and the network.

Radio observations of limb brightening have shown contradictory results. Interferometer observations of Christiansen and Warburton (1953) at 21 cm showed an asymmetric distribution, with strong limb brightening in the E–W but no limb brightening in the N–S. Single dish observations at shorter wavelengths, however, show that the quiet Sun is circularly symmetric (e.g., Kundu and McCullough, 1972) and there is no evidence for the asymmetry observed at 21 cm. However, accurate estimation of limb brightening from these observations has proved difficult mainly because the resolution of single dish telescopes is poor – of the order of 1′ – and the exact beam shape is not well known. Nonetheless, the general results indicate that at $\lambda \gtrsim 3$ cm there is limb brightening, whereas at shorter wavelengths there is controversy as to whether there is limb brightening or darkening (Kundu, 1965, 1982). Since the resolution with the WSRT is $\sim 6''$ (E–W) $\times$ $15''$ (N–S), one should be able to overcome many of the resolution problems encountered with single dish observations.

2.1. Solar Network

The supergranulation network was observed at 6 cm with the WSRT on June 16, 1976 by Kundu *et al.* (1979). Figure 1 shows the ‘clean map’ of the central $10' \times 10'$ field with the radio emission from the plage region McMath 14271 subtracted from the $1\overset{'}{.}5 \times 1\overset{'}{.}4$ box at left center. The ‘clean map’ of Figure 1 reveals low-level structures. The most intense feature on the ‘clean map’ has a 6 cm brightness temperature $\sim 1.7 \times 10^4$ K above the mean solar disk temperature of 2.0×10^4 K. ‘Typical’ bright radio network features in Figure 1 have brightness temperatures $\sim (5 \pm 1) \times 10^3$ K above the mean solar disk temperature of 2.0×10^4 K. Similarly, the regions of low radio brightness in Figure 1 typically have temperatures $\sim (5 \pm 1) \times 10^3$ K below the mean

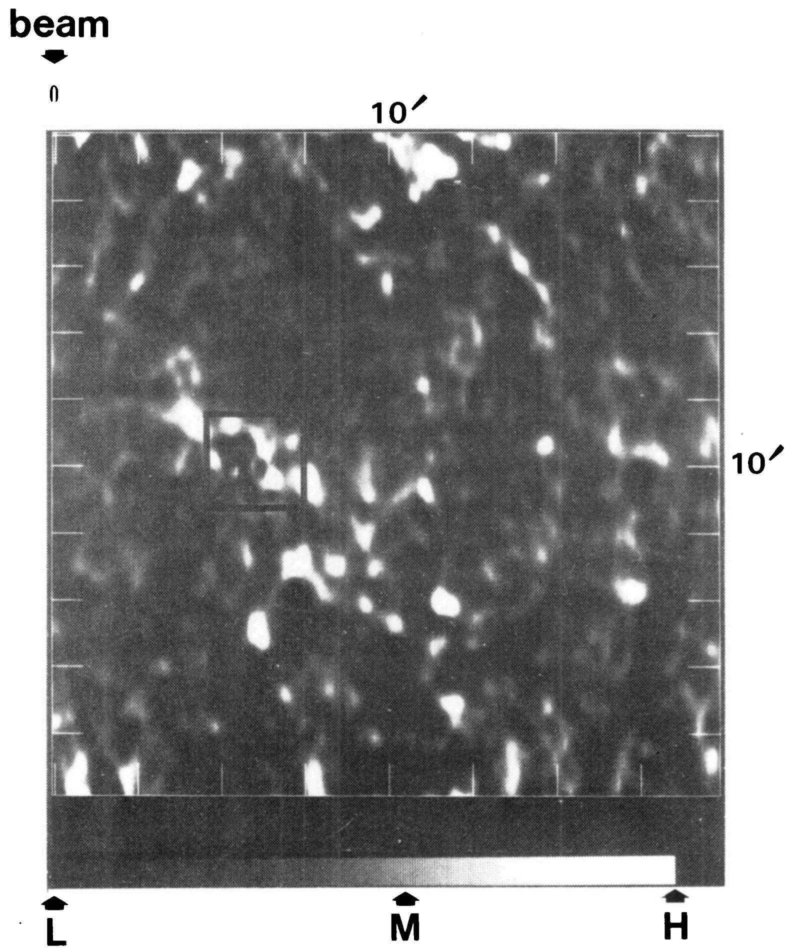

Fig. 1. WSRT 6 cm 12 hr synthesis 'clean map' of 10′ × 10′ central disk field on 1976, June 16. The box indicates the 1′.5 × 1′.4 region from which radio plage MPR 14271 has been subtracted. The gray-scale intensities corresponding to the lowest, mean, and highest brightness temperatures of this map are indicated by L ($T \approx 11 \times 10^3$ K), M ($T \approx 2.2 \times 10^4$ K), and H ($T \approx 3.3 \times 10^4$ K).

solar disk temperature. The typical radio network contrast, defined as

$$\frac{\text{r.m.s. network temperature}}{\text{r.m.s. cell temperature}} \approx (1.7 \pm 0.2):1\,,$$

is consistent with the network contrast of ~2 to 1 found by Reeves (1976) at levels where the mean temperature is $T \approx 2 \times 10^4$ K. Reeves (1976) found that the maximum network contrast (~4:1) occurred at heights where the mean temperature was much greater ($T \approx 2 \times 10^5$ K).

2.1.1. *Comparison between 6 cm Map and Optical Photograph*

Figure 2 shows a digitized and smoothed (over the 6 cm beam) Ca^+K photo for 16 June. A similarly digitized and smoothed 'control' photograph of the central disk region taken in the same Ca^+K line at 14:03 UT on 1976, June 14 was also used. Inspection of Figures 1 and 2 indicates that there is a tendency for the radio and Ca^+K features to be cospatial. The results of a two-dimensional numerical cross-correlation analysis between the radio map and the Ca^+K maps for both June 16 and June 14 are given

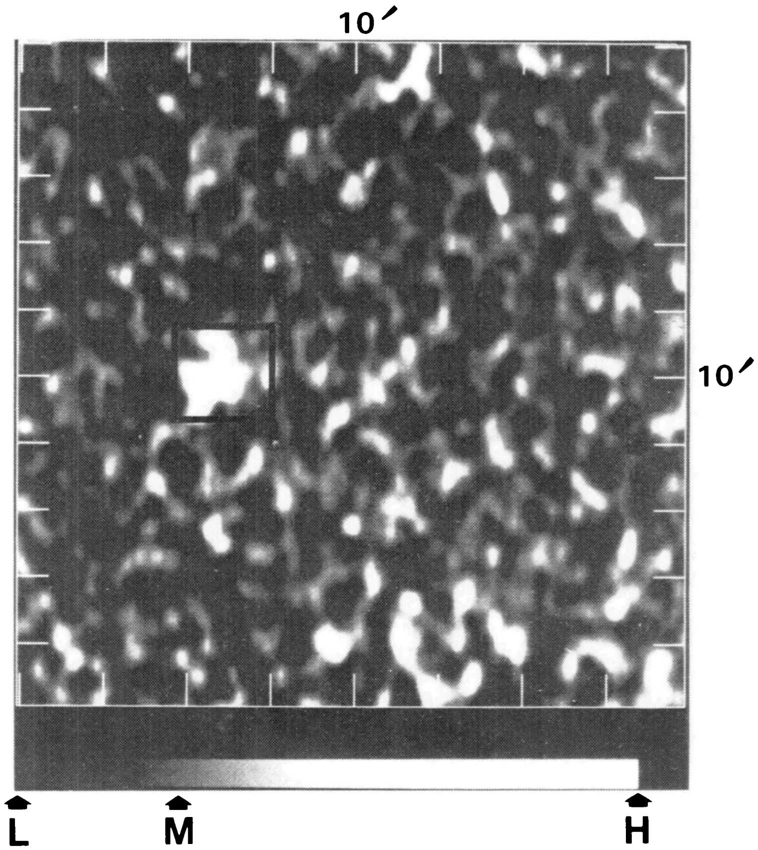

Fig. 2. Sacramento Peak Ca^+K spectroheliogram of 10′ × 10′ central disk region taken at 14:21 UT on 1976, June 16. This map has been digitized and smoothed over a 6″ E–W × 15″ N–S 'beam' to degrade its resolution to that of the 6 cm map of Figure 1. The box indicates 1.′5 × 1.′4 region surrounding MPR 14271 which was deleted during cross-correlation analysis. The gray scale intensities corresponding to the lowest, mean, and highest map intensities in this display are indicated by *L*, *M*, and *H*.

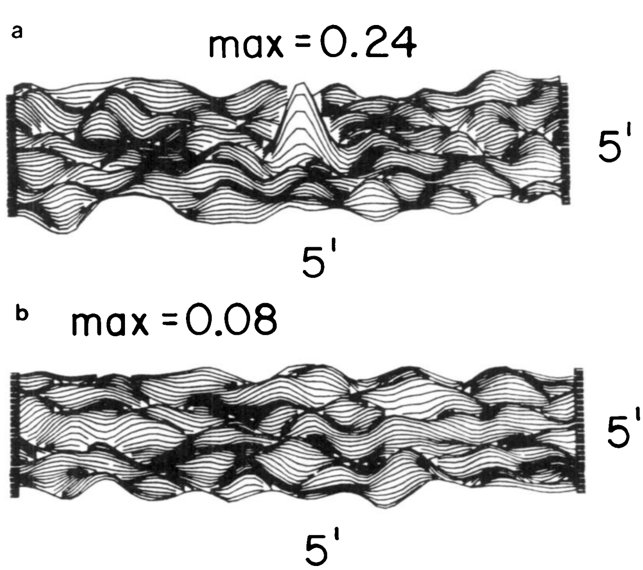

Fig. 3. Two-dimensional cross-correlation of (a) WSRT 6 cm map with same-day Ca^+K and (b) WSRT 6 cm map with 2-day earlier Ca^+K.

in Figures 3(a) and 3(b). Figure 3(a) shows that there is a peak on the positive cross-correlation function (significant at the 3σ level) located within 5″ of the initial guess at the alignment between the 6 cm radio map (Figure 1) and the corresponding Ca^+K map for 1976 June 16 (Figure 2). For comparison, we have performed a two-dimensional cross-correlation between the 6 cm radio map of Figure 1 and the 'control' Ca^+K map of June 14. Figure 3(b) shows that there is no peak in the cross-correlation coefficient higher than the 1σ level for shifts $\lesssim 5'$. The radio versus same-day Ca^+K cross-correlation is likely to be higher than the 3σ level if the radio map could be synthesized in a shorter time. During the 12 h synthesis there is certainly some rearrangement of the supergranulation pattern which is known to have a lifetime of ~20 hr (Simon and Leighton, 1964).

2.1.2. *Spatial Distribution of* 6 *cm Quiet Sun Disk Emission*

The results of an autocorrelation analysis on the radio map of Figure 1, and on the June 16 Ca^+K map of Figure 2 and the June 14 Ca^+K 'control' map are shown in Figures 4(a)–(c). The three autocorrelation displays of Figures 4(a)–(c) all have central

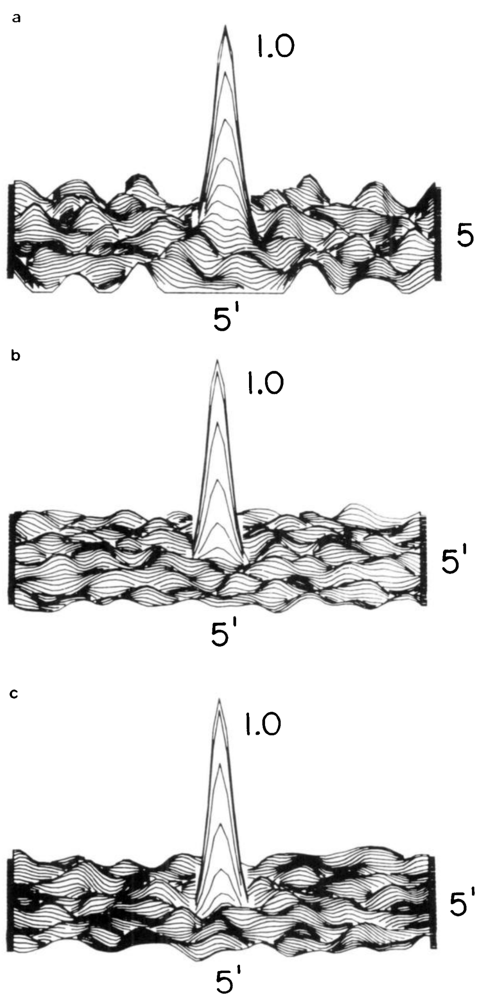

Fig. 4. Two-dimensional autocorrelation for (a) 1976, June 16 WSRT 6 cm map of Figure 1; (b) 1976, June 16 Sacramento Peak Ca^+K map of Figure 2; (c) 1976, June 14 Sacramento Peak Ca^+K 'control' map.

peaks with comparable full width at the 1σ level and secondary peaks within shifts $\lesssim 5'$ of no higher than 1.5σ. The azimuthal average autocorrelation functions about these central peaks are shown in Figures 5(a)–(c). The characteristic 'network width' W estimated from the full width at half-maximum (FWHM) of the central peak of the autocorrelation function $\approx 15''$ ($\sim$11000 km) for the radio map, the Ca^+K map of June 16, and the control Ca^+K map of June 14. Note that the radio and Ca^+K widths

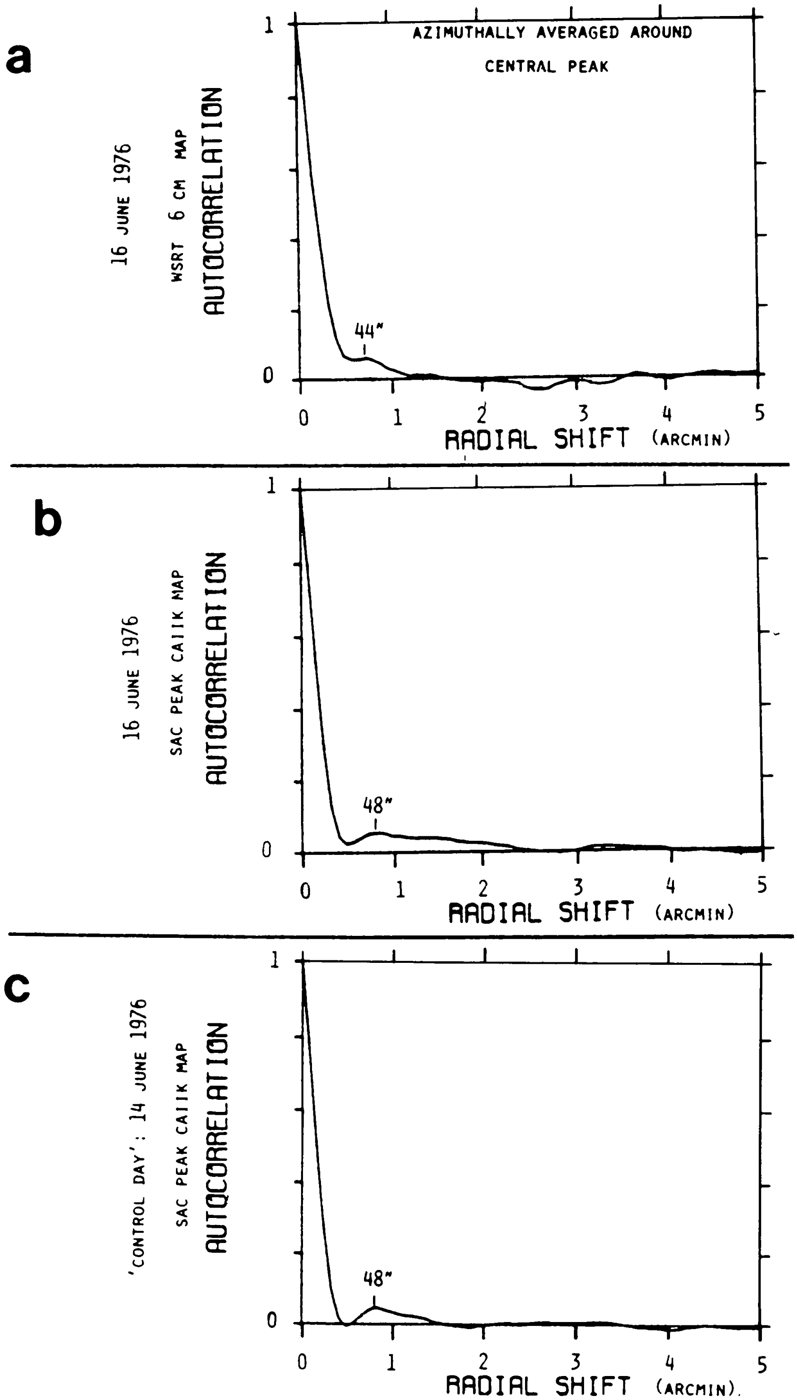

Fig. 5. Autocorrelation of Figures 4(a)–(c) azimuthally averaged around central peak. (a) WSRT 6 cm map of 1976, June 16; (b) Ca^+K map of 1976, June 16; (c) Ca^+K 'control' map of 1976, June 14.

are larger than the width of 10″ found by Reeves (1976) in the EUV. The characteristic cell spacings L estimated from the positions of secondary peaks in Figures 5(a)–(c), are ~44″ for the 6 cm features, and ~48″ for the Ca^+ K features observed on June 16 and June 14.

The above study provides strong evidence that the supergranulation network observed at optical wavelengths can be observed at centimeter wavelengths. The emission at these wavelengths originates partly from the transition region and partly from the corona. Since the network elements do not appear in the coronal EUV lines, we believe that at centimeter wavelengths we are observing only the contribution from the transition region. Using the RATAN-600 radio telescope, at 2–4 cm with ~12″ × 72″ resolution, Pariiskii *et al.* (1976) had previously shown the existence of structures having spatial properties similar to the optical network; however, these results were based upon strip scans with a beam 72″ long. Thus, Kundu *et al.* (1979) produced the first synthesized two-dimensional map of the supergranulation network at radio wavelengths. The temperatures and densities of these structures at higher levels in the transition region and as observed at centimeter wavelengths are of extreme importance for studies of solar atmosphere models.

2.2. Limb brightness distribution

The solar limb was observed in an attempt to synthesize the limb profile and study limb brightening at 6 cm. Four regions on the Sun whose heliocentric coordinates were N 70 E 00 (N limb), N 00 E 70 (E limb), N 00 W 70 (W limb), and S 70 E 00 (S limb) were synthesized on June 17, 1976, using the WSRT. To overcome the difficulty of synthesizing limb brightening due to grating responses and lack of zero and short baselines, Kundu *et al.* (1979) employed two different methods: least-squares fitting and deconvolution. For details see Kundu *et al.* (1979).

Figure 6 shows limb brightening of ~40–50% at the south limb. The peak of the limb brightening is at ~15″ outside the white-light limb, which has a radius of 15′46″ on

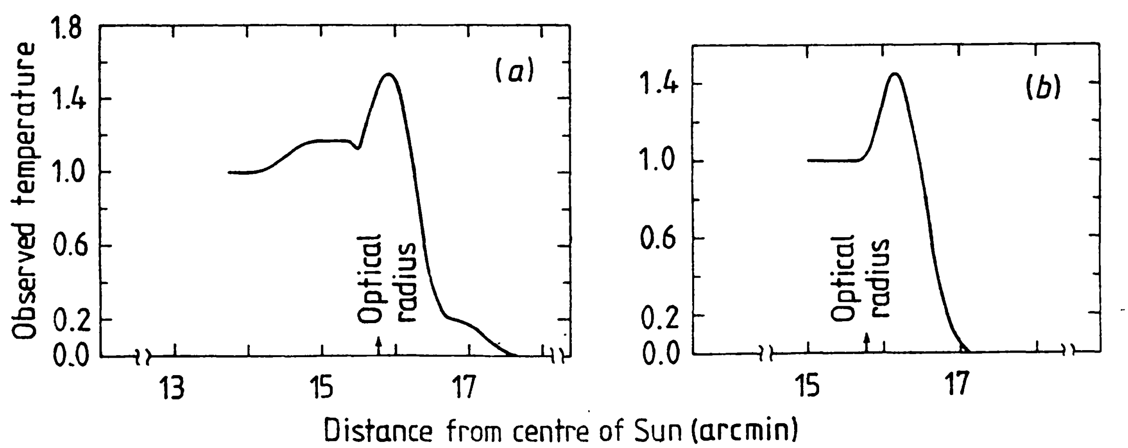

Fig. 6. (a) Limb profile of the south limb, using the deconvolution method. The temperatures have been normalized by the temperature of the disk center; (b) limb profile of the west limb estimated from a two-component least-squares fit.

this day. The west limb also shows clear limb brightening and the limb brightening at the west limb is at a radius larger than that at the south limb by ~15″.

The half-power radius of the Sun at 6 cm is larger than the white-light Sun by ~40″ at the south limb and by ~50″ at the west limb. The observations clearly show limb brightening at both the west and south limbs. This is in contradiction with the earlier results at 9 cm and longer wavelengths which indicate that the Sun shows limb brightening at the east and west limbs, but not at the north and south limbs. A partial explanation of the discrepancy could be that at these wavelengths the observations are affected by the presence of coronal holes at the poles of the Sun which are well known to evolve in both size and density on a time-scale of days to weeks.

3. Observations of Filaments

At centimeter wavelengths, the quiescent prominences seen on the disk appear as depressions in brightness temperature that are well correlated with Hα dark filaments.

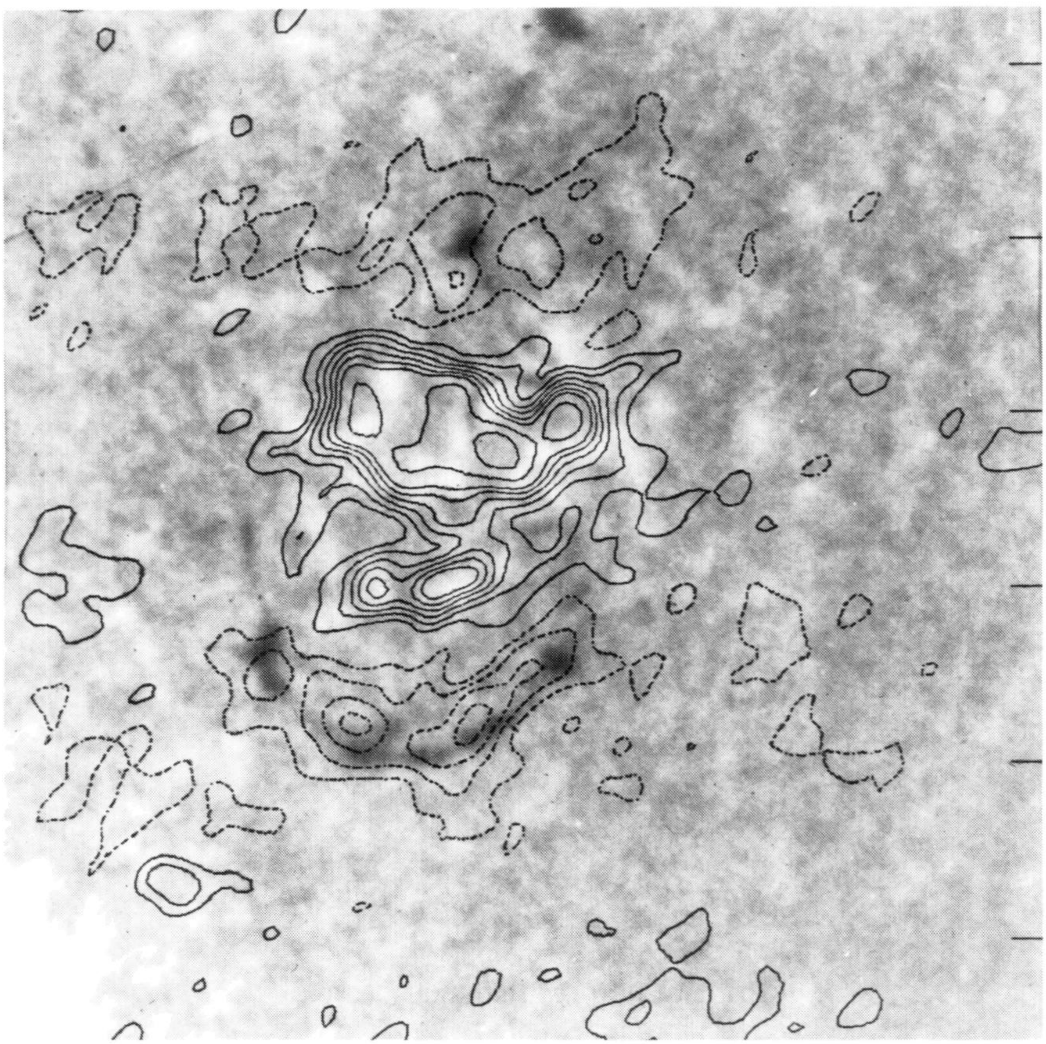

Fig. 7. Radio filament at 6 cm superposed on the corresponding Hα picture (courtesy of Sacramento Peak Observatory).

In a large number of cases, the sizes of the radio and optical filaments are similar (e.g., Schmahl *et al.*, 1981), although in some cases, the radio filaments are found to be broader than the corresponding Hα filaments (see, e.g., Kundu and McCullough, 1972; Kundu *et al.*, 1978). Since the filaments are optically thick they should have the same brightness temperature at radio wavelengths as the electron temperature at optical wavelengths. However, the radio observations indicate that the brightness temperature of a filament increases with wavelength. This has been interpreted as due to radiation from the filament transition sheath where the electron temperature increases from 6000 K at the filament to about 10^6 K, the temperature of the surrounding corona. Accurate determination of filament temperature as a function of wavelength is impor-

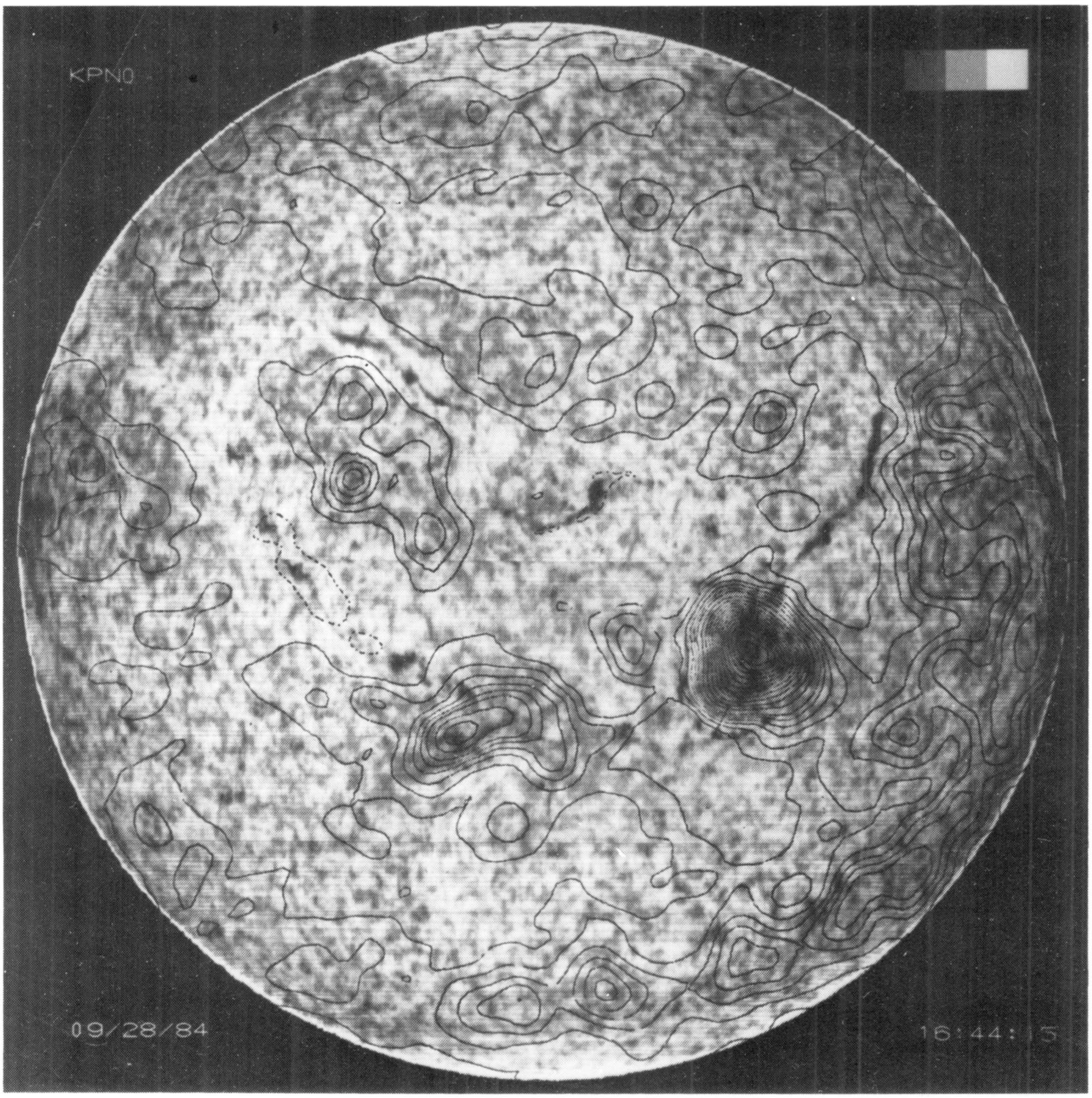

Fig. 8. Radio filament at 20 cm superposed on the He I 10830 Å spectroheliogram of KPNO.

tant, since it can provide information on the density and temperature structure of the filament transition sheath, which in turn determines the amount of thermal energy conducted into the filament from the corona (e.g., Rao and Kundu, 1977). Therefore, it is necessary to produce accurate two-dimensional maps of radio filaments with angular resolution as good as a few arc sec. Rao and Kundu (1980) produced the first synthesized map of a filament at 6 cm with angular resolution of $\sim 15''$, using the WSRT.

Figures 7 and 8 show a disk filament observed with the VLA at 6 and 20 cm, superposed on Hα and He I 10830 Å spectroheliograms, respectively. We see a good correspondence between the 6 cm depression features and Hα filaments, and also between the 20 cm depression features and filaments as well as the lack of emission in the He I picture of KPNO. Typical brightness temperatures of the radio filaments at 20 cm are $\sim 5.7 \times 10^4$ K + 10%. At 6 cm these values are ~ 16000 K $\pm$ 10% (Kundu *et al.*, 1985).

4. Microwave Active Regions

High-resolution microwave observations of solar active regions (e.g., Kundu *et al.*, 1977; Alissandrakis and Kundu, 1982; Lang and Willson, 1982; Chiuderi-Drago *et al.*, 1982) have shown that the slowly varying component of solar radio emission is associated with sunspots, plages and regions of transverse magnetic fields or neutral lines. The strong sunspot associated component at centimeter wavelengths with brightness temperatures of up to a few million degrees has been generally interpreted as arising from emission at low harmonics of the gyrofrequency. The weaker and extended low brightness temperature sources ($T_b \lesssim 10^5$ K) associated with chomospheric plages are usually interpreted as originating from thermal free-free emission from the transition region and corona above active regions. The moderately intense emission ($T_b \gtrsim 10^6$ K), sometimes associated with plages or with regions of transverse magnetic fields (as evidenced by neutral lines) is also attributed, at least in part, to low harmonic gyroradiation.

The total intensity structure of isolated spot associated sources as observed with a resolution of a few arc sec is fairly simple, with emission coming from an area about the size of the peunumbra (Kundu *et al.*, 1977), although some exceptions have been reported (Alissandrakis and Kundu, 1982; Kundu and Alissandrakis, 1984). The circular polarization structure is more complicated; a source with two polarization peaks was observed by Kundu *et al.* (1977), while observations with higher resolution (Alissandrakis and Kundu, 1982; Lang and Willson, 1982) showed that the circular polarization is higher at the edge of the total intensity source, forming a 'ring' or 'horseshoe' structure.

Two model computational studies of the slowly varying component have been made recently, one by Gel'freikh and Lubyshev (1979) and the other by Alissandrakis (1980). The two studies lead to basically the same conclusions: The structure of the source depends upon which of the low order (first to fourth) harmonics of the gyrofrequency are located in regions of high temperature (i.e., in the upper transition region or low corona). This, in turn, depends upon the wavelength and the local value of the magnetic field. Once a given harmonic satisfies the above condition, the intensity of the radiation is determined by its opacity, which has much stronger dependence on the angle θ between the field and the line-of-sight, than on any other physical parameter such as temperature and density.

There is always a region of small opacity, at the location where $\theta \simeq 0$. The extent of the region depends mainly on the harmonic number and the emission mode (ordinary or extraordinary); at 6 cm it is very small for the second harmonic in the ordinary mode and quite extended for the third harmonic in the extraordinary mode. The image of a given harmonic may look like a uniform disk, a disk with a depression corresponding to the low opacity region, or even a crescent. The location of the depression with respect to the rest of the image depends on the heliocentric distance of the source: as the source moves toward the limb, the depression moves from the center of the source toward the center of the disk.

If only the third harmonic is located in a high-temperature region (i.e., when the photospheric field is low and/or the observing frequency is high) there is little emission in the ordinary mode, while the structure of the extraordinary mode map has the form of a ring (if the source is located at the center of the disk) or a thin crescent. Due to the lack of ordinary mode radiation, the source is almost 100% polarized and the total intensity and circular polarization maps are almost identical. When both the third and second harmonics are located above the chromosphere, the resulting image in right or left circularly polarized radiation is a superposition of disks and crescents which gives a peculiar form to the source. The total intensity (I) image retains a form similar to the disk-crescent form of the right and left circularly polarized images, while the circular polarization (V) image has a different form. The circular polarization is low at the locations of high total intensity and shows maxima in regions of intermediate total intensity (Alissandrakis and Kundu, 1984).

The comparison of the observations of a source with the models gives the possibility of inferring which harmonics are responsible for the emission and thus estimating the magnetic field intensity. In this respect the cm wavelength maps can be considered as magnetograms; however, unlike Zeeman magnetograms they do not give the value of the magnetic field at a particular location, but rather the temperature of the region where the magnetic field has a given value. Observations at different frequencies can give the magnetic field as a function of temperature, and this in turn can give the field as a function of height if the variation of temperature with height is known.

5. Determination of Magnetic Fields in the Low Corona

Using the Westerbork Synthesis Radio Telescope (WSRT) at 6.16 cm wavelength Alissandrakis and Kundu (1984) studied a simple bipolar active region (McMath 16382) as it moved from longitude east 50° to west 16°. The region contained two large spots of opposite magnetic flux, with penumbral structure that appeared to rotate clockwise

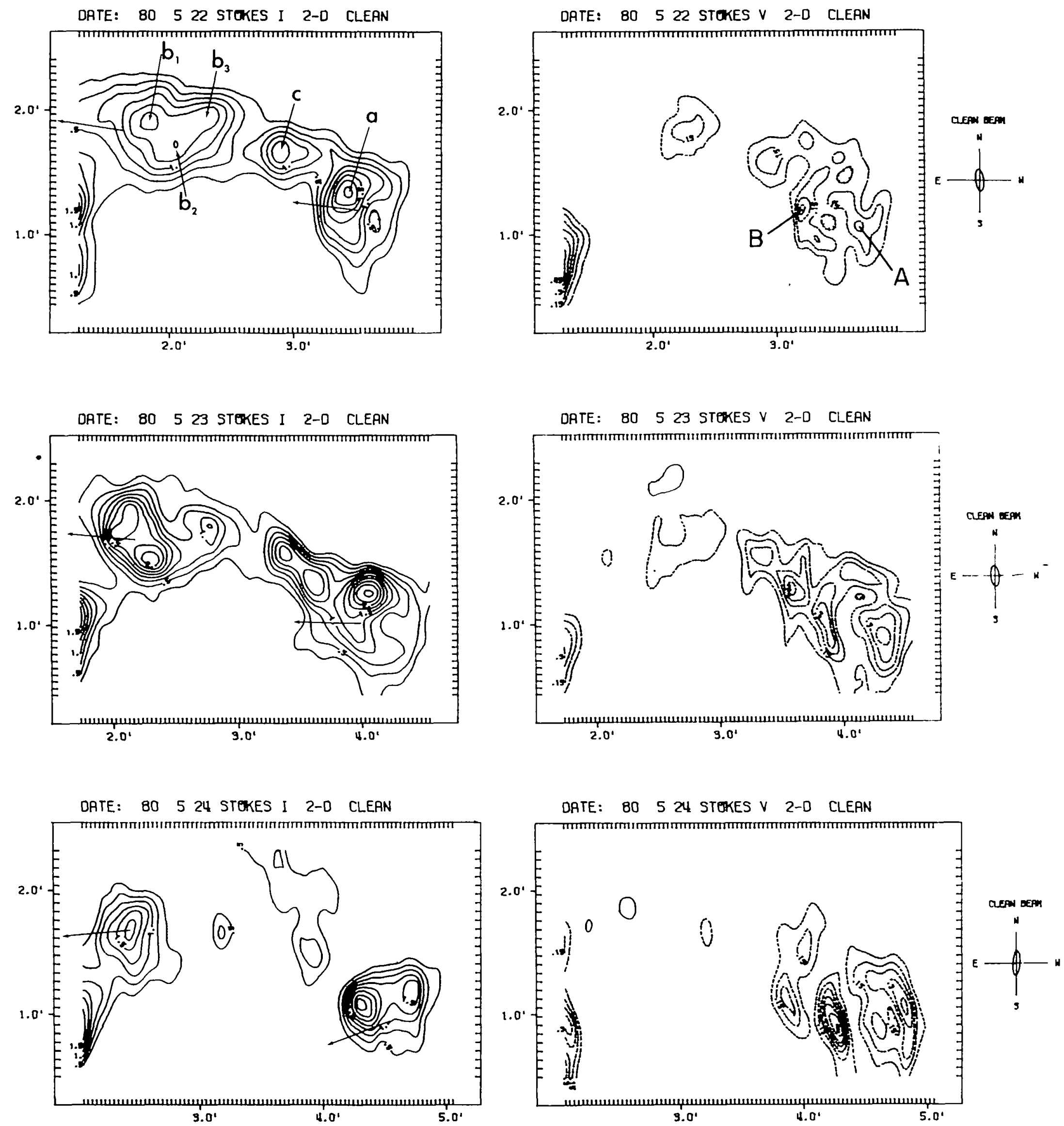

Fig. 9a. 22–24 May, 1980.

Fig. 9a-b. Total intensity and circular polarization maps for McMath region 16862. Celestial north is up, celestial west to the right. The west part of region 16862 is visible near SE corner of the maps. Total intensity contours are in steps of 0.25×10^6 K for I-maps, 0.075×10^6 K for the V-maps; the contour at 0.25×10^6 K has not been drawn on the I-maps of May 24 and 25. The arrows show the direction of the limb.

around the leading spot and counterclockwise around the follower during the six days of observations (May 22–27, 1980). The microwave maps were analyzed in great detail to determine the strength and orientation of the coronal magnetic fields during this period.

The maps showed two prominent sources associated with the two spots and some weak emission between them. As defined by the lowest contours, the sources appeared to be displaced slightly limbward from the spots, indicating that the radio sources were located about 10^4 km (within a factor of 2) above the photosphere. The leading source

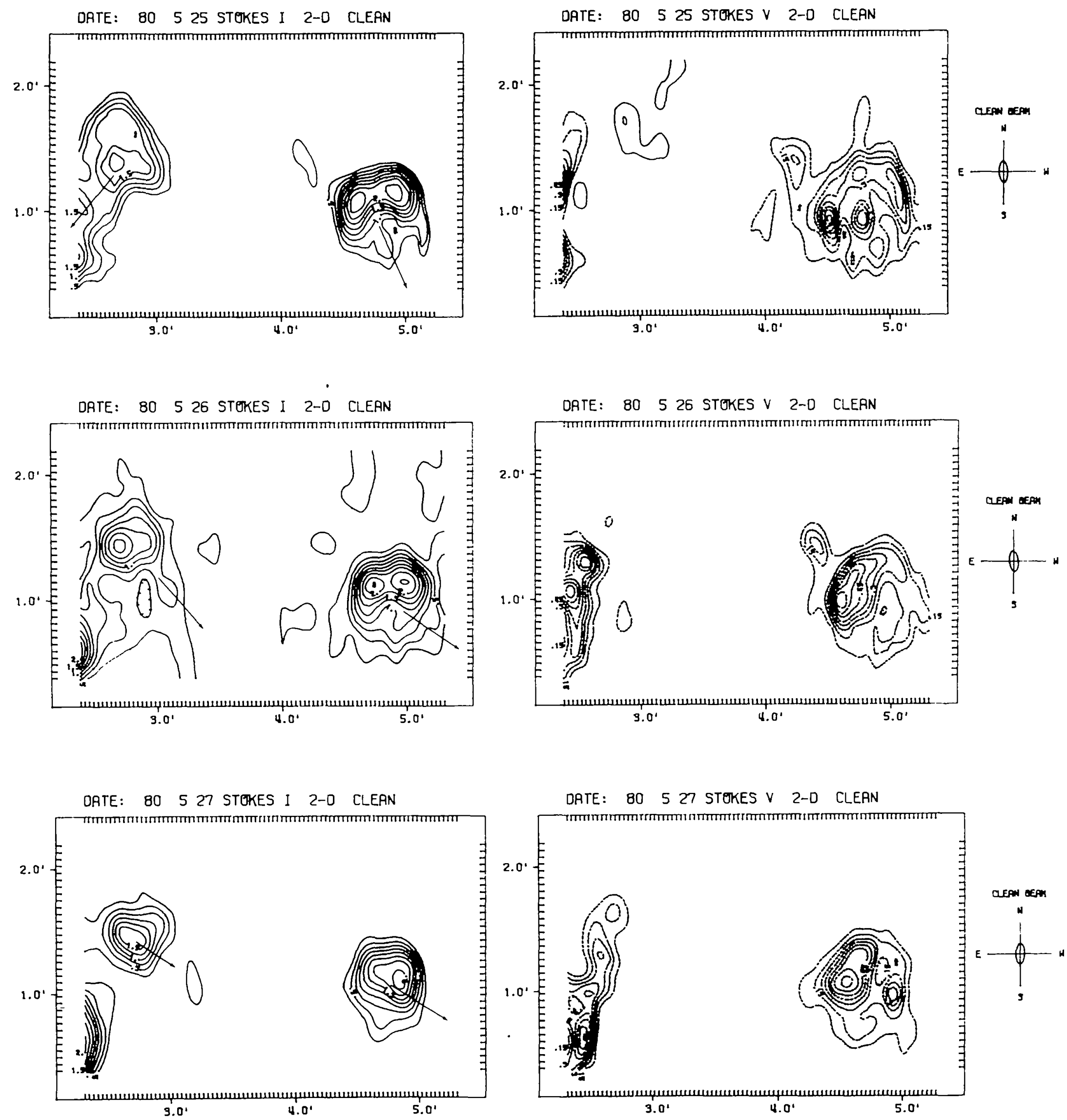

Fig. 9b. 25–27 May, 1980.

appeared roughly elliptical in the lowest contours, much like the leading spot, but the higher contours showed a crescent shape, with the intensity peak displaced in the limbward direction from the centroid of the lowest contours (see Figure 9). The intensity gradient of the convex part of the source, which overlay the penumbra, was greater than that of the concave part, which overlay the umbra. This gradient difference was larger when the spot was farthest from disk center. The peak brightness temperature of the source changed little, from a minimum of 2×10^6 to a maximum of 2.6×10^6 K, and the flux showed a maximum value of 4 s.f.u. near the central meridian.

An interesting question is whether the rotation of the spot has any effect on the shape and structure of the radio maps. Although structural changes give the impression that the source rotated in the clockwise sense throughout the observing period, this is not related to the rotation of the spot itself. It is rather a consequence of the fact that as the position of the source on the solar disk changes, so does the angle between the magnetic field and the linge-of-sight, and consequently the opacity of the harmonic layers. A careful inspection of the maps of May 24 and 25, shows that the source has almost the same shape and structure.

The leading source was left-handed circularly polarized (extraordinary mode) and was apparently unaffected by mode coupling. The structure of the I and V maps leads to the conclusion that both the second and third harmonics are responsible for the emission, otherwise the source would have been almost 100% polarized.

Model calculations of gyroresonance emission from a current-free dipole magnetic field embedded in a plane parallel atmosphere showed a striking similarity with the leading source of May 22 (Figure 10). In the model, the peak brightness of the L-map

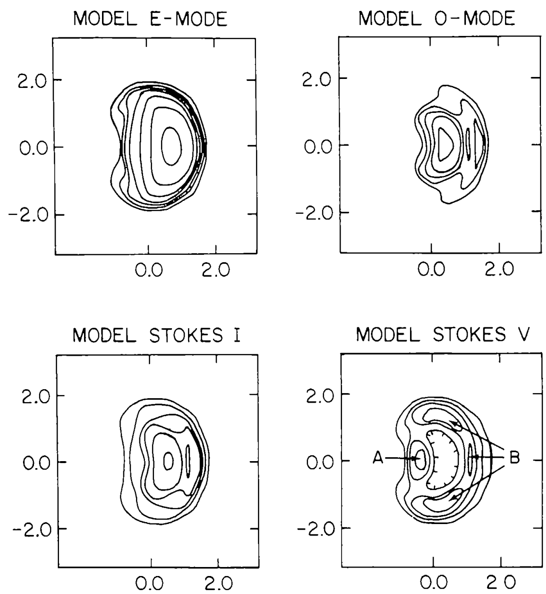

Fig. 10. Computed maps of the extraordinary and ordinary mode radiation, and of total intensity (I) and circular polarization (V) of a sunspot-associated source at 6.16 cm. The magnetic field is that of a vertical dipole placed 2.7×10^9 cm below the base of the transition region with a dipole moment of 1.2×10^{31} c.g.s. units. The temperature structure is determined by a constant conductive flux of 6×10^6 erg cm^{-2} s^{-1} while the pressure is determined by hydrostatic equilibrium and a value of 10^{15} K cm^{-3} at the base of the transition region.

corresponds approximately to the electron temperature of the third harmonic level and the peak brightness of the R-map corresponds approximately to the electron temperature of the second harmonic level. Furthermore, the point where the magnetic field is parallel to the line-of-sight corresponds to the low opacity region where the maps show low intensity and high circular polarization. The angle 1 between the magnetic field vector and the vertical, determined from the maps (Figure 11) showed an almost linear increase as a function of distance from the source center. A plot of the location of the low-opacity region, with the direction and magnitude of the derived horizontal component (Figure 12) showed that the horizontal field had both an azimuthal and a radial component. However, the horizontal component in this model appeared to rotate

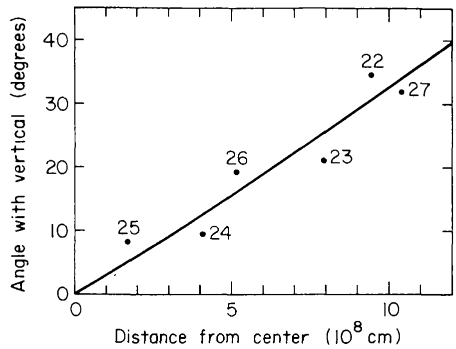

Fig. 11. The angle of the magnetic field vector with the vertical as a function of distance from the center of the source. The solid line is a fit with a force-free model with $\gamma = 1.08 \times 10^{-8}$ cm. The numbers beside the data points are the dates of the observations.

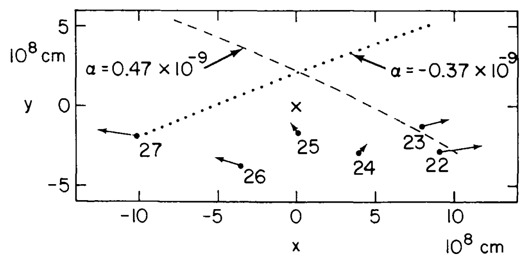

Fig. 12. The position of the low intensity region projected on the horizontal plane. The arrows show the magnitude and direction of the horizontal component of the magnetic field. The $\times$ shows the center of the source. The dashed and dotted lines are loci of computed positions for two values of α.

counterclockwise, rather than clockwise, the direction of the rotation of the spot. In addition, the low opacity region was displaced limbward from spot center, rather than towards disk center, as current-free models predict. Alissandrakis and Kundu (1984) developed a force-free model to explain these discrepancies.

In the I-maps the axis of symmetry of the source is not directed toward the limb, which is an effect produced by a twisted magnetic field, further arguing for a force-free model, for which the analytical model of Schatzman (1961) was used. In this model, the projection of the magnetic field lines on the plane of the sky are logarithmic spirals forming an angle ϕ with the radial direction, and the angle l of the field vector to the vertical is a function of radius only. Both ϕ and l were determined from the maps. A least square fit to l (as estimated from the initial current-free model), combined with the best fit to ϕ yielded the value of the vertical magnetic scale height ($1/k$) and the ratio of the current to magnetic field strength (α).

For May 22–23, $\alpha = 0.47 \times 10^{-9}\ \text{cm}^{-1}$; and $k = 0.98 \times 10^{-9}\ \text{cm}^{-1}$. For May 27, the values obtained were not significantly different, but for May 24 and 25, the model was not suitable, implying almost 90° [180°] twists or negative radial components of the magnetic field. Alissandrakis and Kundu found that the structure of the maps could be reproduced by inclining the dipole axis of a current-free magnetic field by 45° from the vertical. They concluded that the magnetic field structure rotated by about 50°

counterclockwise between May 24 and 25, opposite to the sunspot rotation. The inclined dipole model also fit the other days of observation as did the force-free model.

These high spatial resolution microwave observations show the importance of radio maps for tracing the magnetic field of the low corona, particularly in combination with optical or X-ray observations.

6. Radio Observations of Coronal Loops

The observation of magnetic loops at radio wavelengths is important in view of the apparent abundance of such structures at X-ray wavelengths in the low corona (Rosner *et al.*, 1978). X-ray imaging of the Sun has shown that loops of hot plasma are a major structural component of the low corona. X-ray observations have been particularly useful in understanding the physics of active regions and coronal heating, and in enabling plasma parameters such as pressure and temperature to be determined. However, radio observations have the advantage that they can provide information on the loop magnetic fields, and their gradients along and across the loops, and the magnitude of possible toroidal fields due to electric currents along the loops. Kundu and Velusamy (1980) first reported the existence of a looplike structure connecting two sunspots of opposite polarity in an active region at 6 cm wavelength, and attributed the emission at the foot points ($T_b \sim 5 \times 10^6$ K) located near the sunspot umbra to the gyroresonance process, while the emission in the loop (outside of the foot points) was attributed to optically thin thermal bremsstrahlung ($T_b \sim 10^6$ K). On the other hand, Lang *et al.* (1982) observed a radio loop at 20 cm and attributed all the observed emission to thermal bremsstrahlung. Thus, there appears to be disagreement over the source of optical depth within the loop.

Figure 13 shows the total intensity map of a 20 cm active region (McConnell and Kundu, 1983); the 20 cm sources connect regions of opposite magnetic polarity and, therefore, they must be magnetic loops in the low corona. In order to derive a consistent

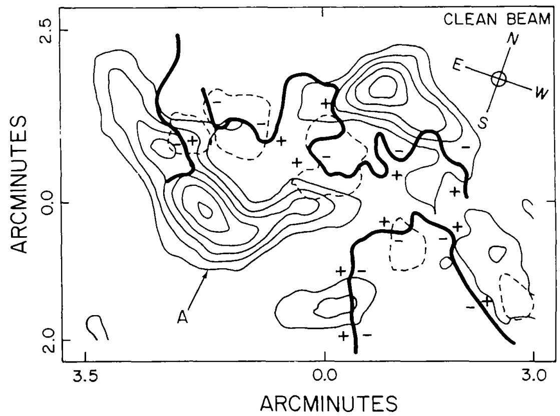

Fig. 13. Map of the 20 cm radio emission from an active region showing two loops. Note that each loop terminates in two regions of opposite polarity. The peak brightness temperature is 1.7×10^6 K, and the contour levels are 15, 30, 45, 60, 75, and 90% of the map maximum. The thick lines indicate neutral lines.

model of the radio emission in loops, McConnell and Kundu used models for active region loops and calculated the expected thermal bremsstrahlung and gyroresonance emissions. They showed that the brightness peak ($T_b \sim 1.7 \times 10^6$ K) of the observed 20 cm loops cannot be due to thermal bremsstrahlung, contrary to the conclusions of Lang *et al.* (1982). However, the secondary maxima near the loop foot points could be explained by thermal bremsstrahlung.

McConnell and Kundu (1983) considered thermal gyroresonance emission as the cause of the emission peak observed near the center of the loop. The magnetic field strength required to give resonance for 20 cm radiation is 170 G or 130 G, depending on whether the third or fourth harmonic dominates. Since the angle (θ) between the line-of-sight and the magnetic field is maximum near the top of the loop and the loop temperature is maximum at the top, thermal gyroresonance emission should peak at the top of the loop provided the magnetic field strength falls in the right range. This was as observed. Indeed, McConnell and Kundu showed that for realistic physical parameters of the loop ($N_e \simeq 5 \times 10^8$ cm^{-3}, $f = 1446$ MHz, $T \simeq 2 \times 10^6$ K and for large θ ($\theta \geqslant 65°$)), the required scale length of magnetic field variation, L_B would be $\gtrsim 2 \times 10^7$ cm and $\gtrsim 5 \times 10^9$ cm for $\tau_{gr} \gtrsim 1$ at the third and fourth harmonics respectively. Both these conditions are plausible but the former is probably more easily satisfied. Thus, the 20 cm loop emission can be explained by a model consisting of two components: a component due to bremsstrahlung which is important near the feet of the loop, and a gyroresonance component which peaks near the top of the loop.

7. Observations of Flares with the VLA

7.1. Spatial structure at 2 and 6 cm wavelengths

In a flare the energy release is usually located in the lower corona and, therefore, the microwave observations can be used to derive the physical parameters in the flaring region such as the electron density, magnetic field strength, and number of gyrosynchrotron emitting electrons. With the high resolution of a few arc sec as presently available with the VLA, it is possible to locate the flare energy release site within the complex magnetic structure of the flaring active region. The observations conducted in the past (e.g., Alissandrakis and Kundu, 1978; Kundu *et al.*, 1982; Marsh and Hurford, 1980) indicate that the radio bursts are generally located over the magnetic neutral line whereas their Hα counterparts are located near the footpoints of the flaring loop. The close association of hard X-ray bursts with the microwave bursts (Kundu, 1961) suggests a common origin of energetic electrons radiating in the two spectral domains.

Simultaneous multifrequency observations in microwaves and hard X-rays are needed to properly understand the radiation mechanisms operating in different spectral domains and are, therefore, important in modelling a flare. Shevgaonkar and Kundu (1985) carried out simultaneous microwave burst observations at 6 and 2 cm with the VLA with spatial resolution of 5″ × 3″ at 6 cm and 2″ × 1.6″ at 2 cm, respectively. Figure 14 shows the time profiles of the burst at 6 and 2 cm and in hard X-rays. At 6

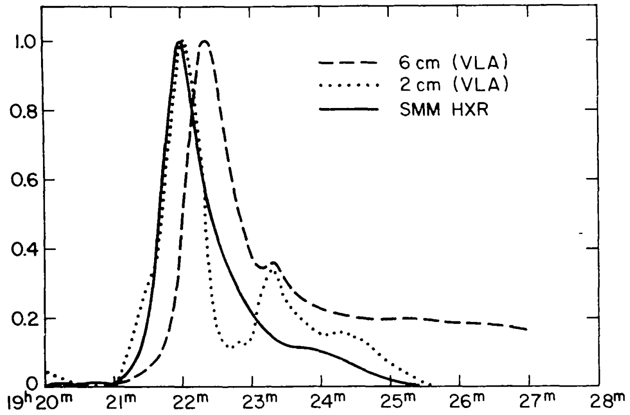

Fig. 14. Flux versus time profiles of the burst. At 6 and 2 cm the shortest baseline of $\sim 2\ k\lambda$ is used. Hard X-ray profile is over an energy range 30–60 keV. The normalization factor is ~ 8.5 s.f.u. at 6 cm and ~ 0.9 s.f.u. at 2 cm. For hard X-ray profile maximum counts are 120.

and 2 cm, the shortest baseline of $\sim 2\ k\lambda$ was used to obtain the time profile. The burst consists of two peaks; the first peak is much stronger than the second one. The hard X-ray and the 2 cm emissions peak more or less simultaneously but the 6 cm peak is delayed by ~ 15 s. Figure 15 shows the total intensity maps at 6 and 2 cm around the peak of the burst. The observed degree of circular polarization was low.

From total intensity maps it is clear that the burst sources at 6 and 2 cm are not co-spatial. The source at 6 cm has its total intensity maximum lying between the two isolated bright components of the 2 cm source. Comparing the source locations with the

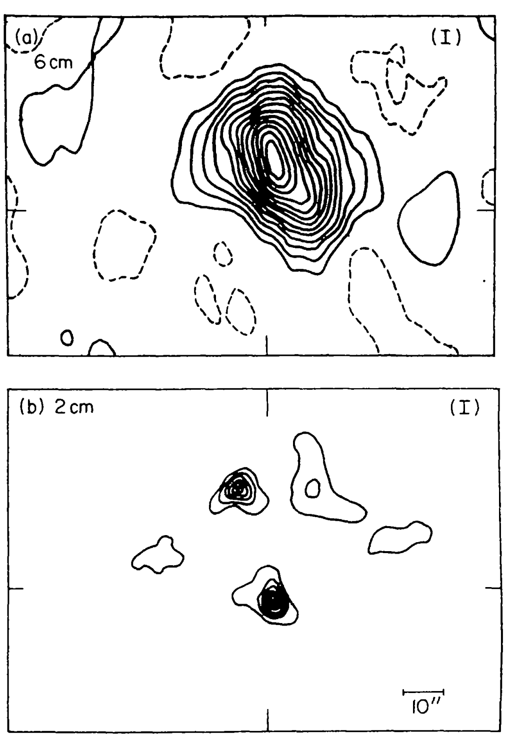

Fig. 15. Total intensity (I) maps around the stronger peak of the burst at 6 and 2 cm. Contour interval is 2.6×10^6 K at 6 cm and 9.70×10^4 K at 2 cm.

magnetic structure of the quiescent active region it is apparent that the 6 cm source more or less overlies the magnetic neutral line whereas, the 2 cm sources coincide spatially with the strong magnetic regions. Moreover, the two components of the 2 cm source lie over the regions of opposite magnetic polarity.

From the spatial locations of the 6 and 2 cm sources within the magnetic structure of the active region it appears that the 6 cm emission originates from the top of the loop in which the flare energy is released while the 2 cm emission arises from the footpoints. The brightness temperatures at 6 and 2 cm are $\sim 4 \times 10^7$ K and $\sim 10^6$ K, respectively. These relatively low brightness temperatures and low degree of circular polarization may imply that the emission is thermal.

It is important to assess the relative contributions of the thermal and nonthermal emissions in the total burst radiation. First we estimate the brightness due to the nonthermal particles produced in the flare. At wavelengths $\lesssim 6$ cm and magnetic fields of a few hundred gauss at the site of flare energy release approximate formulae for gyrosynchrotron emission (Dulk and Marsh, 1982) can be used to compute the brightness temperature.

The computed brightness temperature T_B at 6 cm has been plotted against the magnetic field strength in Figure 16. The values chosen for the microwave source parameters are: density of nonthermal particles $N \sim 10^6$ cm^{-3}, power-law index of the electron energy distribution $\delta = 3$–5, angle between the line-of-sight and the direction of the magnetic field $\theta = 25$ and $70°$, and the strength of the magnetic field $B = 100$–600 G. From Figure 16, it is clear that the emission at 6 cm is optically thin

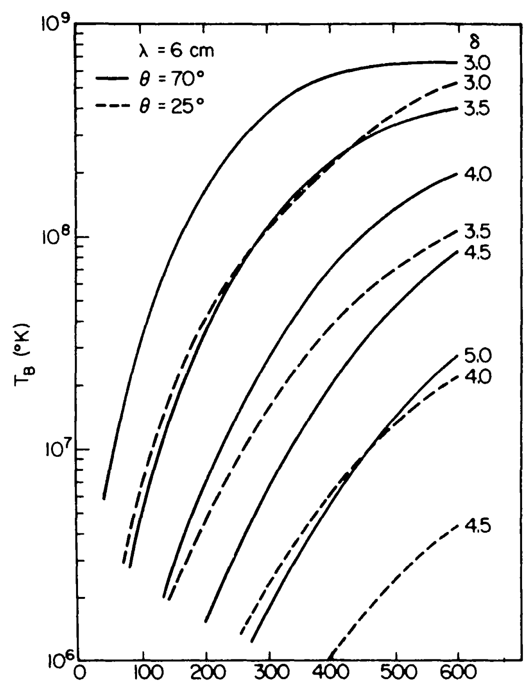

Fig. 16. Brightness temperature due to gyrosynchrotron radiation of nonthermal electrons having a power-law energy distribution versus magnetic field. θ is the angle between the magnetic field and the line-of-sight. δ, power-law index of the energy distribution of the electrons. λ, wavelength used for computations (6 cm).

for the given magnetic field range and, therefore, the degree of polarization p should be $\gtrsim 30\%$ for a magnetic field greater than ~ 100 G. This means that the nonthermal particles, even if they are trapped near the top of the loop, cannot account for the observed low polarization of the 6 cm source. The other possibility is that the 6 cm region is heated to a high temperature of $\sim 4 \times 10^7$ K and the thermal particles produce gyrosynchrotron emission. Using the expression for the absorption coefficient for thermal mildly relativistic electrons (Dulk *et al.*, 1979; Zheleznyakov, 1970) it can be shown that for a density of $\sim 10^{10}$ cm^{-3} of the thermal electrons, the emission is optically thick for a magnetic field of $\gtrsim 200$ G, and the degree of polarization then should be zero. These computations clearly indicate that the observations presented here require that the 6 cm radiation should be dominated by a thermal component. Further, the bulk heated plasma should have a magnetic field of $\gtrsim 200$ G. A similar estimate of the magnetic field in a flaring region was obtained (Velusamy and Kundu, 1981) from the lifetime of electrons in a post-flare loop. If we assume an electron density $\sim 10^9$ cm^{-3}, the lower limit on the magnetic field is slightly increased but the conclusions remain the same.

Since the 6 cm emission originates from near the top of the loop, while the 2 cm emission comes from its footpoints, there should be beaming of nonthermal particles along the magnetic field lines to the footpoints. The possibility of a conduction front moving down the loop is ruled out because in that case the 2 cm emission will peak after the 6 cm emission and, therefore, will not be consistent with the observations. Although the nonthermal particles are beamed to the footpoints, it is not certain if the 2 cm

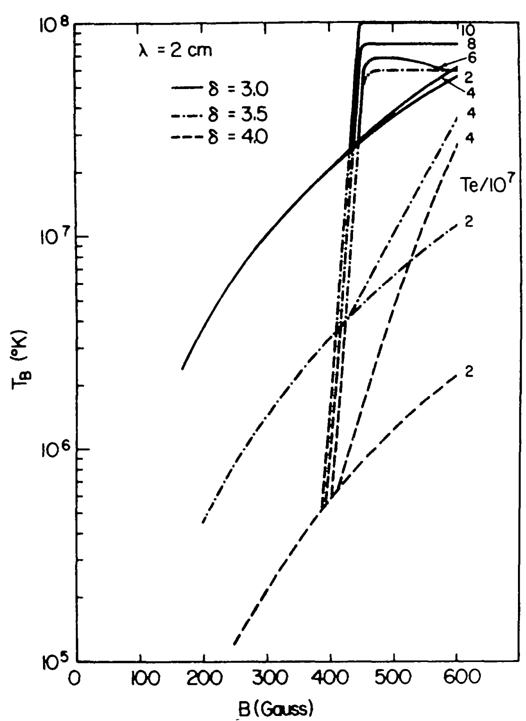

Fig. 17. Brightness temperature at 2 cm from a plasma volume with both thermal and nonthermal particles versus magnetic field. T_e is the thermal temperature of the plasma and δ is the power-law index of the nonthermal particle energy distribution. Angle between the magnetic field and the line-of-sight is 70°.

emission is directly due to gyrosynchrotron radiation of the beaming particles in the high magnetic field, because in that case, due to the small angle θ between the line-of-sight and the magnetic field, one would expect a high degree of circular polarization. A possibility to explain the absence of polarization in the 2 cm source is that the beam of electrons thermalizes in the dense plasma near the footpoints and that the 2 cm emission is due to optically thick gyroresonance radiation in the thermal plasma produced by thermalization of the beam of nonthermal particles. Since the location of the 2 cm sources relative to the 6 cm source supports the presence of nonthermal particles, albeit indirectly, the particles having initial high pitch angles must be present near the top of the loop. From their deficiency to emit at 2 cm in a magnetic field of $\gtrsim 200$ G, we can find from Figure 17 a lower limit on δ to be ~ 4. Even if the nonthermal particles do not produce sufficient emission at 2 cm if $\delta \gtrsim 4$, the thermal component will start contributing to the 2 cm radiation if the magnetic field is $\gtrsim 350$ G (Figure 17). Therefore, from the lack of co-spatiality between the 2 and 6 cm sources and the low degree of polarization in the 6 cm source we estimate a magnetic field of 200–350 G in the flaring region.

7.2. Time delays between 2 and 6 cm burst emission

From Figure 14 it is clear that the 2 cm and hard X-ray burst emissions rise almost simultaneously whereas, for $\sim$ 10–20 s after the onset of 2 cm and hard X-ray emission, the 6 cm emission first rises slowly and then almost as impulsively as the 2 cm emission. A multiple kernel model has been proposed to explain large delays between the peaks of 5 and 15 GHz emission (Brown *et al.*, 1983). In this model the source is assumed to be composed of small kernels with different physical parameters. These kernels flare sequentially to produce mini bursts with much shorter duration whereas, the rise time of the ensemble of the mini bursts could be much longer. The different kernels have different physical parameters and, therefore, different spectral characteristics with the result that the spectral index of the burst changes with time. This change in the spectral index during the burst appears in the form of a pseudo delay.

Although this model is capable of explaining large delays, it requires that the physical conditions must change appreciably from one kernel to another. Further, the multiple kernel model could probably apply to this burst if the burst emission at two wavelengths starts simultaneously but their rise times are different. The initial slow rise and the subsequent impulsive rise at 6 cm cannot be explained by the multiple kernel model. Since we believe the emission at 6 cm to be due to the bulk heated plasma and that at 2 cm due to nonthermal particles, it may be possible to attribute the delay to the time difference between the heating of the plasma and the acceleration of the particles. Several solar flare models propose DC electric field to accelerate the particles (e.g., Holman, 1985). The high currents associated with the electric fields in turn produce Joule heating of the thermal plasma. Assuming the presence of electric fields in the flaring region, the Joule heating time (t_J = rise time at 6 cm) and the nonthermal particle production time (t_N = rise time at 2 cm) can be calculated from the formulae given by Holman (1985).

Since 6 cm emission is believed to be thermal and 2 cm emission due to nonthermal particles, t_J and t_N essentially represent the rise times of the 6 and 2 cm emission respectively. From the observed dimensions of the 6 cm source and a density of 10^{10} cm^{-3}, the total number of thermal particles $N_T \approx 10^{36}$. Taking the area of the current sheet to be equal to the source area and a magnetic field ~ 200 G, the thermal rise time is

$$t_J = 12 \times 10^5 \, \nu_e^{-1} \left(\frac{v_c}{v_e}\right)^2 \text{ s},$$

where v_c = critical velocity = $6\,(n_e/E)^{1/2}$ (cm s^{-1}); v_e is the electron thermal velocity (cm s^{-1}); ν_e is the collision frequency in the current sheet $\approx 300 N_e T_e^{-3/2}$ (s^{-1}); n_e is the density in the current sheet (cm^{-3}); N_e is the density in the thermal plasma (cm^{-3}); E is the DC electric field (statvolt cm^{-1}). Also, during the initial slow rise phase at 6 cm the condition that $t_J > t_N$ requires $v_c/v_e \lesssim 5$ if $N_T/N_r \sim 10^4$; N_r is the total number of accelerated electrons.

Even if we assume $v_c/v_e \sim 2$, a high density of $\sim 2 \times 10^{13}$ cm^{-3} is needed in the current sheet to get the correct order of magnitude for t_J. To overcome this difficulty one can consider (a) the presence of plasma turbulence in the current sheet creating an anomalous resistivity which is many orders of magnitude higher than the classical value and/or (b) multiple current sheets, $\sim 10^4$ as suggested by Holman (1985) to generate nonthermal hard X-rays. However, multiple current sheets alone will not explain the initial slow rise phase. On the other hand, if anomalous resistivity is present at the burst onset, t_J and $t_N \ll 1$ s, there will be no delay and no initial slow rise phase. Therefore, at the burst onset the resisitivity should be classical. The generation of anomalous resistivity depends upon the instabilities which are excited if the drift velocity of the electrons (v_d) exceeds the threshold velocity v_{thr} ($= fC_s$); c_s = ion sound speed and f is a function of the ratio of electron to ion temperature (T_e/T_i). For $T_e \approx T_i$, $f = 35$; $T_e = 8\,T_i$, $f = 8$; and $T_e \gg 10\,T_i$, $f = 1$. Since $v_{\text{thr}} \sim T_e^{1/2}$ and $v_d \sim T_e^{3/2}$ (see Holman, 1985) the ratio $v_d/v_{\text{thr}} \sim T_e$, i.e., as the temperature increases the ratio v_d/v_{thr} increases and after a threshold temperature at which $v_d \approx v_{\text{thr}}$ the instabilities are induced, the resistivity increases greatly and the emission at both wavelengths increases impulsively. In the initial phase, from the relation $v_c/v_e \lesssim 5$ (condition for $t_J > t_N$) and $v_d/v_{\text{thr}} > 1$ (condition for anomalous resistivity) we have $10^{-11} \lesssim E T_e/n_e \lesssim 2 \times 10^{-10}$. For a density of 10^{11} cm^{-3} in the current sheet and $T_e \sim 5 \times 10^6$ K (assuming that at this temperature the anomalous resistivity is generated) we can estimate the electric field in the current sheet as $0.2 \lesssim E \lesssim 4\mu$ statvolt cm^{-1}.

8. Summary

The quiet Sun observations with the WSRT have shown that the 6 cm network has the same scale as the Ca$^+$K network ($\sim 15''$), somewhat larger than the width of the network in EUV. The cell sizes in radio and Ca$^+$K are also identical. The brightness temperature of typical network elements is $\sim 2.5 \times 10^4$ K, while that of the network cells is $\sim 1.5 \times 10^4$ K. The contrast between network elements and cells is, therefore, $\sim 1.7:1$, which compares with $\sim 1.3:1$ for Ca^+K network and $\sim 2:1$ for Lα network. The radius of the 6 cm disk is $\sim 45''$ greater than the white-light Sun. The difference in size is larger than the synthesized beam of the telescope. There is evidence that the equatorial radius of the Sun is greater than the polar radius by $\sim 10''$, but the difference may not be too significant, since it is comparable to the synthesized beam. Limb brightening has been observed on both west and south limbs, and the peak limb temperature is about 40% greater than the temperature of the disk. The presence of limb brightening at the south limb which was not observed by earlier observers, suggests the absence or weakening of polar coronal holes. Using the VLA, we have produced synthesized maps of disk filaments at 6 and 20 cm which correspond well to Hα disk filaments and regions of reduced emission in He I 10830 Å spectroheliograms.

The WSRT observations of 6 cm active regions have premitted us to compare the structure of one sunspot associated source, as well as its center to limb variation with model computations. We have been able to identify features on the radio maps, such as the region where the magnetic field is directed along the line-of-sight. Using a new method of analysis we have been able to map the vertical as well as the horizontal component of the sunspot magnetic field at specific locations in the low corona. The vertical component decreases away from the center of the source, while the horizontal component has both a radial and an azimuthal part. Assuming a plane parallel model for the electron temperature above the spot we interpret these results in terms of a force-free magnetic field model as well as in terms of a dipole with its axis inclined to the vertical. Using the VLA, we have observed coronal loops at 20 cm; the radio emission is attributed to bremsstrahlung near the loop footpoints, whereas gyro-resonance process dominates near the loop top.

Simultaneous VLA observations of a microwave burst at 2 and 6 cm wavelengths show that the 6 cm burst source is located close to a magnetic neutral line, presumably near the top of a flaring loop, while the 2 cm emission originates from the footpoints of the loop. The 6 cm emission is dominated by gyrosynchrotron radiation of the thermal electrons in the bulk heated plasma at a temperature of $\sim 4 \times 10^7$ K, while the 2 cm emission is due to nonthermal particles released and accelerated during the flare process. From the observed low degree of polarization and the lack of the 2 cm source co-spatiality with the 6 cm source a magnetic field of 200–350 G and $\delta \gtrsim 4$ are estimated in the flare energy release site. A DC electric field flare model is invoked to explain the delay of 15 s between the peaks at the two wavelengths. From the delay the strength of the electric field is estimated to be 0.2–4 μ statvolt cm^{-1} in the flaring region.

References

Alissandrakis, C. E.: 1980, in M. R. Kundu and T. E. Gergely (eds.), 'Radio Physics of the Sun', *IAU Symp.* **86**, 101.

Alissandrakis, C. E. and Kundu, M. R.: 1978, *Astrophys. J.*, **222**, 342.

Alissandrakis, C. E. and Kundu, M. R.: 1982, *Astrophys. J.* **253**, L49.

Alissandrakis, C. E. and Kundu, M. R.: 1984, *Astron. Astrophys.* **139**, 271.

Brown, J. C., Mackinnon, A. L., Zodi, A. M., and Kaufmann, P.: 1983, *Astron. Astrophys.* **123**, 10.
Chiuderi-Drago, F., Bandiera, R., Falciani, R., Antonucci, E., Lang, K. R., Willson, R. F., Shibasaki, K., and Slottje, C.: 1982, *Solar Phys.* **80**, 71.
Christiansen, W. N. and Warburton, J. A.: 1953, *Australian J. Phys.* **6**, 190.
Dulk, G. A. and Marsh, K. A.: 1982, *Astrophys. J.* **259**, 350.
Dulk, G. A., Melrose, D. B., and White, S. M.: 1979, *Astrophys. J.* **234**, 1137.
Gel'freikh, G. B. and Lubyshev, B. I.: 1979, *Astron. Zh.* **56**, 562 (*Soviet Astron. – AJ* **23**, 316).
Holman, G. D.: 1985, *Astrophys. J.* **293**, 584.
Kundu, M. R.: 1961, *J. Geophys. Res.* **66**, 4308.
Kundu, M. R.: 1965, *Solar Radio Astronomy*, John Wiley Interscience, New York.
Kundu, M. R.: 1982, *Rep. Progr. Phys.* **45**, 1435.
Kundu, M. R. and Alissandrakis, C. E.: 1984, *Solar Phys.* **94**, 249.
Kundu, M. R. and McCullough, T. P.: 1972, *Solar Phys.* **24**, 133.
Kundu, M. R. and Velusamy, T.: 1980, *Astrophys. J.* **240**, L63.
Kundu, M. R., Alissandrakis, C. E., Bregman, J. D., and Hin, A. C.: 1977, *Astrophys. J.* **213**, 278.
Kundu, M. R., Fürst, E., Hirth, W., and Butz, M.: 1978, *Astron. Astrophys.* **62**, 431.
Kundu, M. R., Melozzi, M., and Shergoonkar, R. K.: 1985, *Astron. Astrophys.*, submitted.
Kundu, M. R., Rao, A. P., Erskine, F. T., and Bregman, J. D.: 1979, *Astrophys. J.* **234**, 1122.
Kundu, M. R., Schmahl, E. J., and Velusamy, T.: 1982, *Astrophys. J.* **253**, 963.
Lang, K. R. and Willson, R. F.: 1982, *Astrophys. J.* **255**, L111.
Lang, K. R., Willson, R. F., and Rayrole, J.: 1982, *Astrophys. J.* **258**, 384.
Marsh, K. A. and Hurford, G.: 1980, *Astrophys. J.* **240**, L111.
McConnell, D. and Kundu, M. R.: 1983, *Astrophys. J.* **269**, 698.
Pariiskii, Yu. N., Korolkov, D. V., Shivris, O. N., Kaidanovskii, N. L., Esepkina, N. A., Zverev, Yu. K., Stotskii, A. A., Akhmedov, Sh. B., Bogod, V. M., Boldyrev, S. I., Gel'freikh, G. B., Ipatova, I. A., Korzhavin, A. N., and Romantsov, V. V.: 1976, *Soviet Astron. – AJ* **20**, 577.
Rao, A. P. and Kundu, M. R.: 1977, *Solar Phys.* **55**, 161.
Rao, A. P. and Kundu, M. R.: 1980, *Astron. Astrophys.* **86**, 373.
Reeves, E. M.: 1976, *Solar Phys.* **46**, 53.
Rosner, R., Tucker, W., and Vaiana, G.: 1978, *Astrophys. J.* **220**, 643.
Schatzman, E.: 1961, *Ann. Astrophys.* **24**, 251.
Schmahl, E. J., Bobrowsky, M., and Kundu, M. R.: 1981, *Solar Phys.* **71**, 311.
Shevgaonkar, R. K. and Kundu, M. R.: 1985, *Astrophys. J.* **292**, 733.
Simon, G. W. and Leighton, R. B.: 1964, *Astrophys. J.* **140**, 1120.
Velusamy, T. and Kundu, M. R.: 1981, *Astrophys. J.* **243**, L103.
Zheleznyakov, V. V.: 1970, *Radio Emission of the Sun and Planets*, Pergamon Press, London.